Available online at http://jprm.sms.edu.pk/
Journal of Prime Research in Mathematics, 22(2) (2026), 82-104

Journal of Prime Research in Mathematics

Tetra-Hybrid Nanofluid Blood Dynamics in Vertical Stenosed Artery with Magnetohydrodynamic and Radiative Insights from the Williamson Model

K. Sudarmozhi[a], V. Sreelatha Devi[a], S. Deepa[b], J. O. Akanni[a,*]

[a]*Department of Mathematics, Saveetha School of Engineering, Saveetha Institute of Medical and Technical Sciences (SIMATS), Chennai, Tamil Nadu, India.*

[b]*Department of Mathematics, Easwari Engineering College, Ramapuram, Chennai, Tamil Nadu, India.*

Abstract

This paper explores the thermo-fluid behavior of tetra-hybrid nanofluid blood flow in a vertical stenosed artery as a non-Newtonian Williamson fluid, accounting for the combined effects of magnetohydrodynamics (MHD), thermal radiation, and double-diffusive effects (Soret, Dufour, and Stefan). The main goal is to measure the sensitivity and interactions of the governing parameters with the engineering responses using sensitivity analysis and response surface methodology (RSM). Similarity transformations are used to convert the governing nonlinear partial differential equations into ordinary differential equations, which are then solved numerically by an iterative scheme with high convergence tolerance. It uses a Central Composite Design (CCD), and statistical analysis is done through ANOVA and a regression model. The Stefan parameter (sb) and the Soret number (Sr) exhibit strong interactions with skin friction and heat transfer. Still, sensitivity analysis suggests that the Stefan parameter (sb) is the dominant factor in thermal transport, and the Williamson parameter (We) is the dominant factor in momentum transport. Moreover, the interaction terms, such as A×C and B×C, make significant contributions to the nonlinear system's behavior. It is noted that growth in the magnetic and Williamson parameters suppresses velocity profiles and amplifies thermal energy due to Joule heating and shear-thinning effects. The results of the research can be applied extensively in biomedical engineering at the time, such as targeted drug delivery, hyperthermia-based therapies, and blood flow control in stenosed arteries. In general, RSM and sensitivity analysis, when integrated, offer a powerful predictive model for optimizing complex biofluid systems.

Keywords: Williamson's fluid, Tetra-hybrid nanofluid, MHD, Artery, Radius of curvature, Thermal radiation.

2010 Mathematics Subject Classification: 05C10, 05C35, 05C57

*Corresponding author

Email addresses: sudarmozhik1033.sse@saveetha.com (K. Sudarmozhi), sreelatu@gmail.com (V. Sreelatha Devi), drdeepraj25@gmail.com (S. Deepa), jide28@gmail.com (J. O. Akanni)

Received : 16 January 2026*; Accepted:* 30 May 2026*; Published Online:* 07 July 2026

1. Introduction

Non-Newtonian nanofluid flow has attracted significant interest in biomedical systems due to its direct applications in hemodynamics, targeted drug delivery, and thermal therapies. Specifically, Williamson fluid models have been shown to describe the shear-thinning behavior of blood under different physiological conditions. Previous studies have mostly addressed analytical and numerical solutions to nonlinear transport equations arising in fluid dynamics and biology, underscoring the importance of accurate representation of momentum and energy transport processes. Nonetheless, most of such studies are restricted to standard fluids or single-phase nanofluid models.

The mathematical modeling of complex fluid systems has been widely explored; however, several limitations remain when extending these models to realistic biomedical flows. Chu et al. [7] developed a fractional multi-dimensional Navier–Stokes framework that improves the theoretical understanding of fluid transport. Yet their formulation is largely mathematical and does not account for non-Newtonian biofluid behavior, nanoparticle effects, or heat-transfer mechanisms. The observed behavior in the current study can be attributed to the findings of Sudarmozhi et al. [25], who analyzed the thermal and flow properties of tetra-hybrid nanofluids in the presence of the Stefan effect. Similarly, Agarwal et al. [2] analyzed biological partial differential equations using semi-analytical techniques, but their study is limited to simplified models that do not consider MHD effects or complex geometries. In another contribution, Rashid et al. [20] proposed an analytical approach based on the Caputo operator; however, their work lacks practical relevance to physiological flows and ignores thermal and radiative transport phenomena.

Recent trends have shifted toward hybrid and multi-hybrid nanofluids, which make a remarkable contribution to thermal conductivity and energy transport properties. Research on hybrid nanofluid convection and Joule heating indicates that the interplay between magnetic fields and nanoparticle composition is the primary factor governing the velocity and temperature distributions. Moreover, research on tetra-hybrid nanofluids indicates that increased nanoparticle complexity improves heat transfer performance at the cost of increased flow resistance and nonlinear rheological effects. Although these developments have been made, the overwhelming majority of the literature addresses the effects of parameters in a more isolated or purely descriptive fashion, without a systematic quantification of parameter sensitivity and interaction.

From a broader modeling perspective, Adel et al. [1] introduced a fractional-order model for COVID-19 dynamics, and Shams et al. [23] developed efficient numerical schemes for nonlinear equations; although mathematically robust, these studies are not tailored to fluid flow or heat transfer problems, limiting their applicability in nanofluid-based biomedical systems. Likewise, Agarwal et al. [3] and Zhang et al. [26] provided theoretical contributions to heat equations and impulsive differential systems. Still, their formulations remain abstract and do not address fluid–thermal coupling or real-world geometrical constraints. In addition, Jamal et al. [14] presented solutions for fuzzy heat and diffusion equations; however, the lack of physical validation and fluid-interaction analysis limits their relevance to engineering applications. Similarly, Al-Dhaifallah et al. [4] applied machine learning techniques to heat exchanger systems, but their work focuses on industrial processes and does not consider nanofluid rheology or biomedical flow conditions.

The strength of the Lorentz force in magnetohydrodynamic (MHD) biofluid systems is regulated by the and the Lorentz force opposes fluid motion. It promotes the expansion of thermal energy (Joule heating). The parameter that defines the non-Newtonian shear-thinning behavior is the Williamson parameter, which directly affects the effective viscosity and velocity retardation. accounts for thermal energy exchange via radiative heat flux, which is important in biomedical procedures involving high temperatures, such as hyperthermia therapy. Moreover, the quantifies the relative importance of momentum diffusivity to thermal diffusivity, thereby determining the thickness of thermal boundary layers. Geometric complexity is introduced by , which affects centrifugal effects on the stenosed arterial configuration, secondary flow structures,

and enhanced convective heat transfer. These parameters are a set that describe a highly coupled, nonlinear system that determines the behavior of flow and heat transfer.

With advances in nanofluid research, attention has shifted toward hybrid systems for enhanced heat transfer. Ali et al. [5] demonstrated improved thermal performance of hybrid nanofluids under magnetic fields; however, their study is limited to conventional hybrid mixtures and does not consider higher-order nanoparticle combinations. Parida et al. [18] examined MHD hybrid nanofluid flow with thermo-solutal effects, but their assumption of Newtonian fluid behavior restricts applicability to blood flow. Similarly, Khan et al. [16] incorporated Joule heating and chemical reactions, yet their analysis is confined to simple geometries and neglects curvature effects relevant to arterial flows. More advanced studies on multi-hybrid nanofluids have shown improved thermal characteristics. Sudarmozhi et al. [25] investigated tetra-hybrid nanofluids and reported enhanced heat-transfer performance; however, their model is limited to isothermal conditions and does not account for MHD or radiative effects. Rehman et al. [21] explored Marangoni convection in nanofluids but did not consider stenosed or curved geometries. Furthermore, Rehman et al. [22] analyzed MHD hybrid nanofluids with radiation, yet their work does not extend to tetra-hybrid systems or evaluate interactions among parameters in detail.

Even though some of these parameters have been studied separately by other researchers, especially in MHD hybrid nanofluids and vertical stenosed artery models, the resulting interpretations tend to be qualitative graphical representations without adequate quantification of the relative effect or interaction strength of each parameter. More recent articles that use statistical tests such as ANOVA and Sobol indices argue that sensitivity analysis is necessary to identify the most influential parameters and enhance the accuracy of predictive modeling. Nonetheless, these methods remain rare in the context of tetra-hybrid nanofluid blood flow under the combined effects of MHD, radiation, and curvature.

In recent years, sensitivity analysis has emerged as an important tool for quantifying the influence of parameters. Farahani et al. [10] employed Sobol-based sensitivity analysis for thermal systems; however, their work is limited to photovoltaic applications and lacks fluid dynamic complexity. Panda et al. [17] used ANOVA techniques to study hybrid nanofluids, but their model is restricted to engineering devices rather than biomedical flows. Similarly, Shoaib et al. [24] analyzed sensitivity in MHD Casson nanofluids, yet their study is limited to hybrid nanofluids and excludes curvature and radiation effects. Ramamoorthi et al. [19] investigated entropy generation in stenosed arteries using sensitivity analysis. However, their work is closer to biomedical applications; it does not incorporate tetra-hybrid nanofluids or Williamson fluid behavior. Additionally, Kasali and Ajadi [15] examined elastico-viscous nanofluids with sensitivity analysis, but their study assumes simple geometries and neglects radiative heat transfer.

*1.1. **Aim and Objective***

To examine the thermo-fluid dynamics of the Williamson tetra-hybrid nanofluid blood flow in a vertical stenosed artery under sensitivity analysis and response surface methodology.

- To simulate the MHD, radiation, Soret, Dufour, and Stefan effects on blood flow.
- To reduce governing equations to the dimensionless form by using similarity variables.
- To optimize with RSM-based design using CCD design.
- To measure the effects of parameters with sensitivity analysis.
- To measure an engineering parameter like skin friction and Nusselt number.

*1.2. **Gap and Novelty in Research***

- Absence of experiments that use tetra-hybrid nanofluid + Williamson model + vertical stenosed artery geometry.

- Little has been done in the simultaneous incorporation of MHD, radiation, Soret, and Stefan effects.
- Lack of quantitative sensitivity and RSM analysis of biomedical nanofluid flow systems.
- Initial experiment of tetra-hybrid nanofluid with complete multi-physics coupling.
- CCD-based RSM + sensitivity analysis of biomedical flow.
- The effects of interaction (We, sb, Sr) on engineering outputs are quantified.
- Concentrate on vertical cylinder geometry, which enhances physiological relevance.

1.3. ***Research Questions***

- What is the joint influence of MHD and Williamson parameters on the velocity of blood flow?
- How do Stefan and Soret parameters compare to each other in terms of their effects on heat transfer?
- What are the dominant interactions between the parameters that dominate skin friction and Nusselt number?
- Is RSM an appropriate predictor of nonlinear thermo-fluid behavior?
- Sensitivity of engineering responses to parameter changes?

1.4. ***Real-Time Applications***

- Drug delivery systems.
- Hyperthermia-based cancer treatment
- Stenosed arteries: Blood flow control.
- Biomedical cooling/heating devices
- Design of nano-enhanced biofluid transport systems

2. Mathematical Modeling

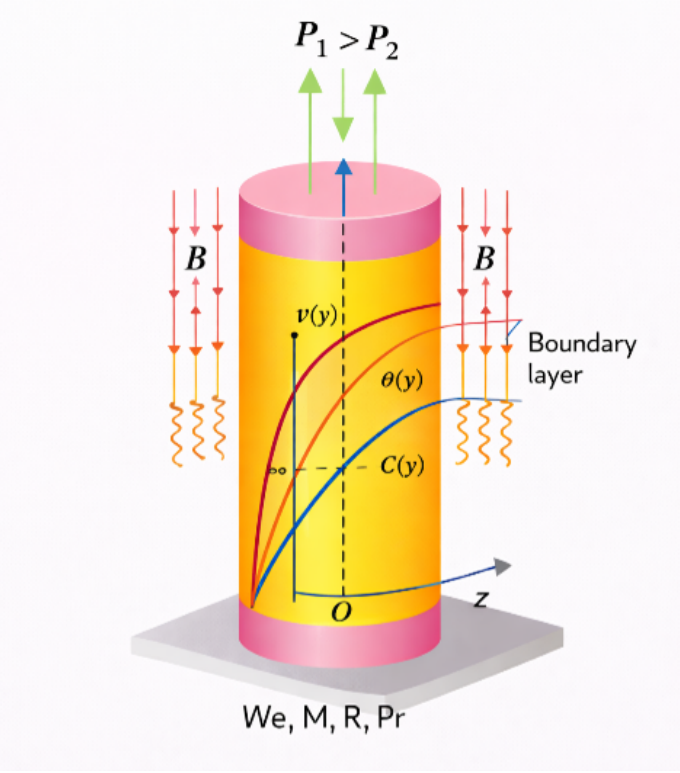

Figure 1: **Schematic Diagram**

This analysis is performed in cylindrical polar coordinates, with the radial coordinate r taken as the radius. r is the distance offset from the point of the cylinder, and the z coordinate is used along the length of the cylinder being stretched, such that r and z intersect at the origin, and the radius of the cylinder is measured to be d. The boundary conditions are such that at the surface of the cylinder ($r = \frac{d}{2}$) the velocity must be parallel to the stretching speed along the length axis, and temperature (T) and concentration (C) are kept constant values (T_w, C_w) which are under a tendency to approach the ambient values (T_∞, C_∞) at a far off distance. The magnetic field influences physical quantities, and thermal radiation affects heat transfer. The current work assumes a constant, laminar flow on a vertically oriented cylindrical surface of constant radius **R**. The axial coordinate z is followed along the length of the cylinder, and the radial coordinate r is measured perpendicular to the surface. The curvature effect in this case arises from the cylinder's geometry and is reflected in the radial dependence of the governing equations. In contrast to vertical stenosed artery models, the cylinder radius is held constant, and no axial geometry changes are accounted for. This equation is a conservation of mass of an incompressible fluid in cylindrical coordinates. It makes sure that the net mass flux in the flow field is also constant. The equation is a momentum balance including the viscous, magnetic (Lorentz force), and non-Newtonian Williamson effects. It describes the evolution of velocity under the combined effects of fluid rheology and an external magnetic field. This equation describes heat transfer in the fluid, accounting for thermal conduction and radiant heat flux. It accounts for the effects of temperature differences and radiation on the thermal boundary layer.
The study has limitations, which are listed below.

- Makes the assumption that the flow is laminar and steady, disregarding the behavior of pulsatile blood.
- Applies Rosseland approximation, which is only valid in optically thick fluids.
- Ignores chemical reactions and biological complexities of actual blood.
- Restricted to certain parameter values (We, sb, Sr).
- Validation is done numerically, but there is no experimental validation.

The following equation models mass transfer by diffusion in the fluid [13]. It is the change in the concentration field, controlled by species transport processes.

$$\frac{\partial}{\partial z}(ru) + \frac{\partial}{\partial r}(rw) = 0 \tag{1}$$

This is the mass-transfer equation associated with diffusion in the fluid.

$$u\frac{\partial u}{\partial z} + w\frac{\partial u}{\partial r} = \frac{\mu_{tethnf}}{\rho_{tethnf}}\left[\frac{\partial^2 u}{\partial r^2} + \frac{1}{r}\frac{\partial u}{\partial r} + 2^{\frac{1}{2}}\Gamma\frac{\partial u}{\partial r}\frac{\partial^2 u}{\partial r^2} + \frac{\Gamma}{r\,2^{\frac{1}{2}}}\left(\frac{\partial u}{\partial r}\right)^2\right] - \frac{\sigma_{tethnf}B_0^2}{\rho_{tethnf}}u \tag{2}$$

It is the fluctuations of the concentration field under the influence of species transport processes.

$$u\frac{\partial T}{\partial z} + w\frac{\partial T}{\partial r} = \left(\frac{k_{\text{tethnf}} + \frac{16\sigma^* T_\infty^3}{3k^*}}{(\rho C_p)_{\text{tethnf}}}\right)\left[\frac{\partial^2 T}{\partial r^2} + \frac{1}{r}\frac{\partial T}{\partial r}\right] + \frac{1}{(\rho C_p)_{\text{tethnf}}}\left(\frac{\partial u}{\partial r}\right)^2 + \frac{D_{\text{tethnf}}\,k_{c_1}}{c_s\,c_p}\left[\frac{\partial^2 C}{\partial r^2} + \frac{1}{r}\frac{\partial C}{\partial r}\right] \tag{3}$$

To incorporate thermal radiation effects into the energy equation, the Rosseland diffusion approximation is employed, which is valid for optically thick fluids. According to this approximation, the radiative heat flux is modeled as

$$q_r = -\frac{4\sigma^*}{3k^*}\frac{\partial T^4}{\partial r}$$

where σ^* is the Stefan – Boltzmann constant and k^* is the mean absorption coefficient. Assuming that temperature differences within the flows are sufficiently small, the term T^4 is linearized using a Taylor series expansion about the ambient temperature T_∞, such that .

$$T^4 \approx 4T_\infty^3 T - 3T_\infty^4$$

This simplification allows the radiative heat flux to be expressed in terms of the temperature Gradient, thereby reducing the energy equation to a more tractable form and enabling effective coupling between conduction and radiation mechanisms. The radiative heat flux in the current research is calculated by the Rosseland approximation, which considers thermal radiation as a diffusion process. This is an approximation that holds when the fluid medium is optically thick, i.e., when the mean free path of photons is significantly smaller than the characteristic length scale of the system.

Moreover, the linearization of the T^4. The use of Taylor series expansion to justify the use of the term is justified when the temperature differences in the flow are small enough. In this case, the higher-order terms may be disregarded, and the radiative heat flux is proportional to the temperature Gradient. Also, the fluid is considered gray and non-scattering, with a constant absorption coefficient. These assumptions guarantee that the Rosseland approximation gives a good description of radiative heat transfer in the boundary layer. Thus, the radiation model adopted is physically valid in the regime of moderate temperature variations and optically dense fluid systems.

These are conditions that characterize the physical limitations at the wall and far-field region of the flow.

$$u\frac{\partial C}{\partial z} + w\frac{\partial C}{\partial r} = D_{\text{tethnf}}\left[\frac{\partial^2 C}{\partial r^2} + \frac{1}{r}\frac{\partial C}{\partial r}\right] + \left[\frac{D_{\text{tethnf}}\, k_T}{c_s c_p}\left(\frac{\partial^2 T}{\partial r^2} + \frac{1}{r}\frac{\partial T}{\partial r}\right)\right] \tag{4}$$

In this way, the stenosis geometry is explicitly defined by a smooth analytical function, and curvature effects are parameterized, ensuring that both geometric and physical effects are always present in the model.

$$\begin{aligned} &u = u_w, w = \frac{D}{1-C_w}\frac{\partial C}{\partial r}, \quad T = T_w, \quad C = C_w \quad \text{at } r = \mathcal{R}, \\ &u \to 0, \quad T \to T_\infty, \quad C \to C_\infty \quad \text{as } r \to \infty. \end{aligned} \tag{5}$$

2.1. ***Similarity variables***

The similarity transformations used in the current study depend on the presence of self-similarity behavior in the boundary layer of a vertical cylinder. Similarity under certain physical and mathematical conditions remains possible despite the geometry introducing curvature and constriction effects. First, the flow is presumed to be axisymmetric, steady, and laminar, eliminating both temporal and angular dependencies. The velocity of the arterial wall is assumed to be proportional to the axial coordinate, such that the velocity field varies in the same way along the direction of flow. Second, the stenosis is supposed to be mild and smoothly varying, so that the geometric effect can be regarded as a perturbation, as opposed to a dominant deformation. This enables the flow to have a locally self-similar structure. In the same way, the curvature of the artery is accounted for by introducing a dimensionless curvature parameter, which does not alter the similarity form but only modifies the governing equations. Third, the external influences, such as the magnetic field, thermal radiation, and double-diffusion, are assumed to be spatially homogeneous. This guarantees that no additional spatial dependence is introduced into the system, thereby preserving the similarity transformation. With these assumptions, the governing partial differential equations reduce to a set of ordinary differential equations in terms of a similarity variable. The ensuing formulation embodies the necessary physics of curvature and stenosis and is mathematically tractable.

$$M_1^* = \frac{\mu_{tethnf}}{\mu_f}, \quad M_2^* = \frac{\rho_{tethnf}}{\rho_f}, \quad M_3^* = \frac{\sigma_{tethnf}}{\sigma_f}, \quad M_{11}^* = \frac{(\rho\beta)_{tethnf}}{(\rho\beta)_f}, \quad \alpha = \left(\frac{\nu_f l}{c_1 \mathcal{R}^2}\right)^{\frac{1}{2}},$$
$$M = \frac{\sigma_f l B_0^2}{\rho_f c_1}, \quad M_4^* = \frac{k_{tethnf}}{k_f}, \quad M_5^* = \frac{(\rho C_p)_{tethnf}}{(\rho C_p)_f}, \quad M_6^* = \frac{D_{tethnf}}{\mu_f}, \quad Pr = \frac{\nu_f (\rho C_p)_f}{k_f},$$
$$R = \frac{16\sigma^* T_\infty^3}{3k_f k^*}, \quad B_u = \frac{g\,\beta_0\,(T_w - T_o)\,l}{c_1\,u_w}, \quad Ec = \frac{u_w^2}{(C_p)_f (T_w - T_0)}, \quad u = \frac{c_1 z}{l} f'(\eta),$$
$$Sr = \frac{D_{tethnf}\,k_T}{c_s\,c_p}\left(\frac{C_w - C_\infty}{T_w - T_\infty}\right), \quad Df = \frac{D_{tethnf}\,k_c}{c_s\,c_p}\left(\frac{T_w - T_\infty}{C_w - C_\infty}\right) \quad w = -\frac{\mathcal{R}}{r}\sqrt{\frac{c_1 \nu_f}{l}}\, f(\eta),$$
$$\theta(\eta) = \frac{T - T_\infty}{T_w - T_0}, \quad \eta = \sqrt{\frac{c_1}{v_f l}}\left(\frac{r^2 - \Re^2}{2\Re}\right) \tag{6}$$

2.2. ***Dimensionless Equations***

This equation indicates the dimensionless version of the transformed momentum equation. It highlights the influence of the key parameters, the magnetic field, and the Williamson number, on velocity.

$$\left(\frac{M_1^*}{M_2^*}\right)\left[(1+2\alpha\eta)f''' + 2\alpha f'' + We(1+2\alpha\eta)^{1.5} f'' + \frac{3\alpha We(1+2\alpha\eta)^{0.5} f''^2}{2}\right]$$
$$-f'^2 + ff'' - \left(\frac{M_3^*}{M_2^*}\right) M f' = 0 \tag{7}$$

This equation describes the temperature distribution in a nondimensional form. It highlights the importance of the Prandtl number and the radiation parameter in thermal transport.

$$\left[\frac{M_4^* + R}{M_5^* Pr}(1+2\alpha\eta)\theta'' + 2\alpha\theta'\right] + \frac{M_1^*}{M_5^*}(1+2\alpha\eta) Ec\, f''^2 + f\theta' + M_6\left(Df(1+2\alpha\eta)\,\phi'' + 2\alpha\,\phi'\right) = 0 \tag{8}$$

This equation describes the concentration distribution after non-dimensionalization. It demonstrates the effect of the Schmidt number on mass diffusion properties.

$$\frac{M_6(1+2\alpha\eta)\phi'' + 2\alpha\phi'}{Sc} + f\phi' + M_6\left(Sr(1+2\alpha\eta)\,\theta'' + 2\alpha\,\theta'\right) = 0 \tag{9}$$

2.3. ***Non-dimensional Boundary Condition***

These conditions are equivalent to those for the transformed system when using similarity variables.

$$f(0) = \frac{sb}{Sc}\,\phi'(0), \quad f'(0) = 1, \quad \theta(0) = 1, \quad \phi(0) = 1,$$
$$f'(\infty) = 0, \quad \theta(\infty) = 0, \quad \phi(\infty) = 0. \tag{10}$$

2.4. ***The Properties of Tetra Hybrid Nanofluid***

Thermophysical properties of blood and nanoparticles are borrowed from the literature of Choi [6], Das [8], Eastman et al. [9], Fung [11], and the CRC Handbook of Chemistry and Physics [12].

Table 1: **The Properties of Tetra Hybrid Nanofluid**

Properties	Blood	Gold (Au)	TiO_2	Silver (Ag)	Al_2O_3
ρ	1050	19300	4250	10500	3970
C_p	3617	129	690	235	765
K	0.52	315	8.953	429	40
σ	0.7	$4. \times 10$	2.4×10^{-6}	6.3×10^{7}	3.5×10^{-10}

2.5. ***Physical Thermo Characteristics***

From the literature of Choi [6], Das [8], Eastman et al. [9], Fung [11], and the CRC Handbook of Chemistry and Physics [12].

$$\mu_{tethnf} = \mu_f \left[(1-\phi_1)^{2.5}(1-\phi_2)^{2.5}(1-\phi_3)^{2.5}(1-\phi_4)^{2.5}\right]^{-1},$$

$$\rho_{tethnf} = (1-\phi_1)\left\{(1-\phi_2)(1-\phi_3)\left[(1-\phi_4)\rho_f + \rho_4\phi_4\right] + \rho_3\phi_3 + \rho_2\phi_2\right\} + \rho_1\phi_1,$$

$$(\rho C_p)_{tethnf} = (1-\phi_1)\left\{(1-\phi_2)(1-\phi_3)\left[(1-\phi_4)(\rho C_p)_f + (\rho C_p)_{s4}\phi_4\right] + (\rho C_p)_{s3}\phi_3 + (\rho C_p)_{s2}\phi_2\right\} + (\rho C_p)_{s1}\phi_1,$$

$$\frac{k_{tethnf}}{k_{nf}} = \frac{k_1 + 2k_{nf} - 2\phi_1(k_{nf}-k_1)}{k_1 + 2k_{nf} + \phi_1(k_{nf}-k_1)}, \qquad \frac{k_{tethnf}}{k_{nf}} = \frac{k_2 + 2k_{nf} - 2\phi_2(k_{nf}-k_2)}{k_2 + 2k_{nf} + \phi_2(k_{nf}-k_2)},$$

$$\frac{k_{tethnf}}{k_{nf}} = \frac{k_3 + 2k_{nf} - 2\phi_3(k_{nf}-k_3)}{k_3 + 2k_{nf} + \phi_3(k_{nf}-k_3)}, \qquad \frac{k_{tethnf}}{k_{nf}} = \frac{k_4 + 2k_{nf} - 2\phi_4(k_{nf}-k_4)}{k_4 + 2k_{nf} + \phi_4(k_{nf}-k_4)}.$$

$$\frac{\sigma_{tethnf}}{\sigma_{nf}} = \frac{(1+2\phi_4)\sigma_4 + (1-2\phi_4)\sigma_{tethnf}}{(1-\phi_4)\sigma_4 + (1+\phi_4)\sigma_{tethnf}}, \qquad \frac{\sigma_{tethnf}}{\sigma_{nf}} = \frac{(1+2\phi_3)\sigma_3 + (1-2\phi_3)\sigma_{nf}}{(1-\phi_3)\sigma_3 + (1+\phi_3)\sigma_{nf}},$$

$$\frac{\sigma_{nf}}{\sigma_f} = \frac{(1+2\phi_2)\sigma_2 + (1-2\phi_2)\sigma_f}{(1-\phi_2)\sigma_2 + (1+\phi_2)\sigma_f}, \qquad \frac{\sigma_{nf}}{\sigma_f} = \frac{(1+2\phi_1)\sigma_1 + (1-2\phi_1)\sigma_f}{(1-\phi_1)\sigma_1 + (1+\phi_1)\sigma_f},$$

2.6. ***Skin friction, Nusselt and Sherwood numbers represent fundamental physical parameters***

$$C_f = \frac{2\tau_w}{\rho_{tethnf}u_w^2}, \qquad Nu_x = \frac{xq_w}{k_{tethnf}(T_w - T_\infty)u_w^2}, \qquad Sh = \frac{j_w l}{D},$$

$$\tau_w = \mu_{tethnf}\left(\frac{\partial u}{\partial r}\right)\left\{\frac{1}{1+\left(\Gamma\frac{\partial u}{\partial r}\right)^n}\right\}, \qquad q_w = -k_{tethnf}\frac{\partial T}{\partial r} + q_r, \qquad j_w = -D_{tethnf}\frac{\partial C}{\partial r},$$

The wall drag force in the dimensionless form is given as

$$C_f Re_x^{1/2} = \frac{1}{M_1}\left(\frac{f'}{1+(We\, f'')^n}\right).$$

Nusselt number in the dimensionless form is represented as

$$Nu_x\, Re_x^{-\frac{1}{2}} = -\left\{M_5 + R\left[1+(\theta-1)\theta\right]^3\right\}\theta'.$$

Sherwood number in the dimensionless form is represented as

$$Sh = -\frac{\partial C}{\partial \phi}.$$

3. Methodology

In the current paper, the steady, laminar flow of a tetra-hybrid nanofluid under the influence of magnetohydrodynamics (MHD), thermal radiation, and double-diffusive convection is considered in a vertical stenosed artery. Governing nonlinear partial differential equations, which model conservation of mass, momentum, energy, and species concentration, are developed in cylindrical coordinates and reduced to a system of coupled ordinary differential equations through suitable similarity transformations. The resulting BVP is solved numerically using an iterative method with a high convergence tolerance to ensure solution accuracy and stability. A Central Composite Design (CCD) is used to systematically analyze the impact of essential parameters within the framework of Response Surface Methodology (RSM). Minitab software is used to conduct statistical tests, namely Analysis of Variance (ANOVA), regression analysis, and model adequacy tests, to determine the significance of parameters and their interactions. Additionally, a sensitivity analysis is performed on the partial derivatives of the regression equations to determine the relative effects of the governing parameters on the engineering responses, including skin friction and the Nusselt number. The numerical solution of the boundary value problem is obtained with the help of the bvp4c solver of MATLAB. The numerical solution is the foundation for generating data used in sensitivity analysis and Response Surface Methodology (RSM). The solver is run with reasonable tolerance parameters to guarantee convergence and numerical stability. As the main emphasis of the current work is on statistical analysis and parameter sensitivity, grid independence and numerical convergence are not discussed in detail. However, the solutions obtained are smooth and consistent, thereby validating the numerical results. The default tolerance settings of bvp4c (RelTol $= 10^{-5}$, AbsTol $= 10^{-7}$) were used, which are sufficient for the accurate solution of boundary layer problems

3.1. ***Flow Chart***

Figure 2: **Flow Chart for the methodology**

4. Result and Discussion

4.1. ***A Sensitivity Analysis of Skin Friction and Nusselt Number through CCD-Based Response Surface Methodology.***

In this subsection, a sensitivity analysis of the skin friction coefficient (Sf) and Nusselt number (Nu) is presented using experimental data generated via a Central Composite Design (CCD). The research employs Response Surface Methodology (RSM) to systematically assess the effects of key governing parameters on thermal and flow properties. Three independent variables are taken into account in the analysis: the Williamson fluid parameter We (A), which defines the behavior of non-Newtonian fluids; the Stefan parameter sb (B), which reflects the effects of phase change and heat transfer; and the Soret number Sr (C), which characterizes the mass diffusion caused by temperature gradients. These parameters have been chosen because of their considerable influence on momentum and heat transfer in complex fluid systems.
The two main variables of response are considered:

- Skin friction coefficient (Sf): a measure of the shear stress on the wall and flow resistance.
- Nusselt number (Nu): indicating the rate of heat transfer at the surface

To measure the relationships between inputs and responses, statistical methods such as analysis of variance (ANOVA), regression modeling, and model adequacy checks are used. All computations and model fittings are performed in Minitab to ensure they are statistically well-validated and have accurate predictive capability.

Summary of Design and Methodology of the Experiment.

A Central Composite Design (CCD) is used to construct the experimental framework. It is the ideal design for building second-order polynomial models and capturing curvature effects in response surfaces. Its design is a two-level factorial design with additional axial and center points to improve prediction accuracy. **The design features are:**

- Software used: Minitab to generate design, regression, and ANOVA.
- Number of factors: 3 (We, sb, Sr)
- Total experimental runs: 20
- Alpha (α): 1.68179 (ensuring rotatability of the design)
- Cube (factorial) points: 8
- Center points in cube: 6 (to estimate experimental error and test model adequacy)
- Axial (star) points: 6 (to represent quadratic effects)
- Center points in axial portion: 0

This systematic arrangement allows effective exploration of the parameter space, with minimal experiments required. It also aids in constructing sound empirical models for predicting Sf and Nu under different operating conditions.

Parameters	**Symbols**	**-1**	**0**	**1**
We	A	0.4	0.65	0.9
sb	B	0.10	0.13	0.16
Sr	C	0.1	0.55	1.0

Table 2: **Coded and actual levels of input parameters.**

Statistical Analysis (ANOVA): Table 3 presents the Analysis of Variance (ANOVA) for the skin friction coefficient (C_f) and indicates the statistical significance and adequacy of the developed model. The model shows a very high degree of significance, as the F-value of 10922.45 and the p-value of 0.000 are both significant and not due to random variation. Moreover, every model term, including linear, quadratic (square), and two-way interaction effects, is statistically significant at the 5% significance level $p < 0.05$. This illustrates that it is not just individual parameters that determine skin friction behavior; the interactions among parameters are also important. The importance of higher-order terms also reveals nonlinear relationships among the input variables and the response. All in all, these findings demonstrate the model's soundness and forecasting potential, which are relevant to the analysis and optimization of skin friction properties within the study's parameter range.

Source	DF	Adj SS	Adj MS	F-Value	P-Value	Significant
Model	9	38.6030	4.2892	10922.45	0.000	yes
Linear	3	8.8447	2.9482	7507.65	0.000	yes
A	1	2.8642	2.8642	7293.55	0.000	yes
B	1	5.9762	5.9762	15218.44	0.000	yes
C	1	0.0043	0.0043	10.95	0.008	yes
Square	3	2.9689	0.9896	2520.10	0.000	yes
A*A	1	1.5017	1.5017	3824.16	0.000	yes
B*B	1	0.1176	0.1176	299.36	0.000	yes
C*C	1	1.7467	1.7467	4447.97	0.000	yes
2-Way Interaction	3	26.7893	8.9298	22739.60	0.000	yes
A*B	1	0.1397	0.1397	355.68	0.000	yes
A*C	1	10.7660	10.7660	27415.47	0.000	yes
B*C	1	15.8837	15.8837	40447.64	0.000	yes
Error	10	0.0039	0.0004			
Lack-of-Fit	5	0.0039	0.0008			
Pure Error	5	0.0000	0.0000			
Total	19	38.6069				

Table 3: **ANOVA table for Skin friction** (C_f)

The model summary shows an excellent fit with R-sq = 99.99%, R-sq(adj) = 99.98%, and R-sq(pred) = 99.92%, indicating that the model explains almost all the variability in the response.

Regression Equation in Uncoded Units:

$$C_f = -8.443 + 16.508\,We - 2.19\,sb - 5.0145\,Sr - 5.1649\,We^2 + 100.35\,sb^2 - 1.7192\,Sr^2$$
$$-17.618\,We \cdot sb - 10.3117\,We \cdot Sr - 104.375\,sb \cdot Sr$$

Experimental Outcomes: Table 4 presents the complete experimental design matrix, including both coded and actual values of the three input parameters, i.e., We (A), sb (B), and Sr (C), as well as the experimental results for the skin friction coefficient (C_f). The table provides an overview of all 20 experimental runs performed under the Central Composite Design (CCD). Having both coded and actual values enables one to identify variations in design-space parameters easily, and the respective (C_f) values indicate how the response would behave under varying conditions. This organized data is used as a basis for further statistical analysis, model construction, and validation using response surface methodology.

The Table 4 experimental outcomes for the responses are correlated with the factor levels.

Run	Coded values			Actual values			$C_f(Re_x)^{0.5}$	$Nu_x(Re_x)^{-0.5}$
	A	B	C	We	sb	Sr		
1	-1	-1	-1	0.4	0.10	0.1	-4.5613	2.4513
2	1	-1	-1	0.9	0.10	0.1	-1.0609	1.7772
3	-1	1	-1	0.4	0.16	0.1	-4.1763	2.3450
4	1	1	-1	0.9	0.16	0.1	-1.2045	2.2385
5	-1	-1	1	0.4	0.10	1.0	-23.8823	2.6779
6	1	-1	1	0.9	0.10	1.0	-25.0222	3.1742
7	-1	1	1	0.4	0.16	1.0	-29.1336	1.3359
8	1	1	1	0.9	0.16	1.0	-30.8020	2.3998
9	-1	0	0	0.4	0.13	0.55	-15.1805	2.0628
10	1	0	0	0.9	0.13	0.55	-14.2646	2.2577
11	0	-1	0	0.65	0.10	0.55	-12.9607	1.7083
12	0	1	0	0.65	0.16	0.55	-15.6581	1.2680
13	0	0	-1	0.65	0.13	0.1	-2.5183	1.7948
14	0	0	1	0.65	0.13	1.0	-26.9775	1.9888
15	0	0	0	0.65	0.13	0.55	-14.3998	1.6201
16	0	0	0	0.65	0.13	0.55	-14.3998	1.6201
17	0	0	0	0.65	0.13	0.55	-14.3998	1.6201
18	0	0	0	0.65	0.13	0.55	-14.3998	1.6201
19	0	0	0	0.65	0.13	0.55	-14.3998	1.6201
20	0	0	0	0.65	0.13	0.55	-14.3998	1.6201

Table 4: **Experimental design with coded and actual values**

Model Adequacy Checking: The sufficiency and trustworthiness of the model developed for the skin friction coefficient (C_f) are rigorously assessed using residual analysis, as depicted in Figures 3 These diagnostic plots confirm the statistical assumptions and ensure that the model closely represents the physical behavior of the flow system. The normal probability plot of the Cf residuals is shown in Figure 3a. The data points lie very close to a straight line, indicating that the residuals are normally distributed. Physically, it implies that the deviations between the predicted and observed values are due to random experimental errors rather than systematic errors, thereby demonstrating that the physics of momentum transport in the fluid system has been correctly modeled.

Figure 3b depicts the residuals against fitted values. Homoscedasticity (constant variance) is evident from the lack of no apparent pattern and the random distribution of the points. It means that the model is consistently predictive across all operating conditions. Practically, in biomedical fluid flow (e.g., blood flow in stenosed arteries) or in non-Newtonian fluid processing in factories, this guarantees that the model reliably predicts wall shear stress even when key parameters change.

Figure 3c shows that the residual histogram is symmetric and bell-shaped, supporting the assumption of normality. This is stochastic due to experimental measurements, and it confirms that there is no external bias or other physical phenomenon that significantly affects the results.

Lastly, Figure 3d shows the residuals versus the order of observation. There is no clear trend or cyclical behavior, indicating that the residuals are free of autocorrelation and independent. Physically, this implies that the experimental run will not be dependent on the past conditions and therefore the system is stable, and the measurements will not be subject to time-dependent effects or experimental drift. Overall, the results of these diagnostic processes confirm the statistical validity and physical consistency of the proposed model. This increases trust in its applicability to real-time engineering issues, such as optimizing heat and mass transfer systems, improving biomedical flow predictions, and designing efficient thermal-fluid devices where precise estimation of skin friction is essential.

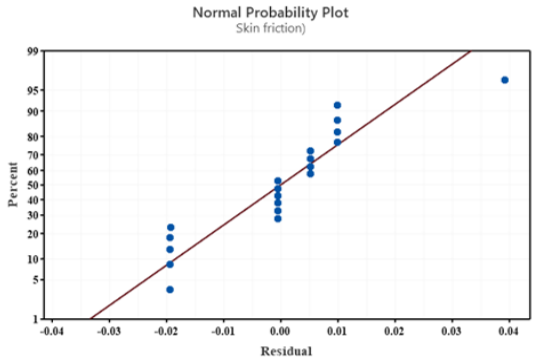

(a) Normal probability plot of residuals for $\mathbb{C}_f$

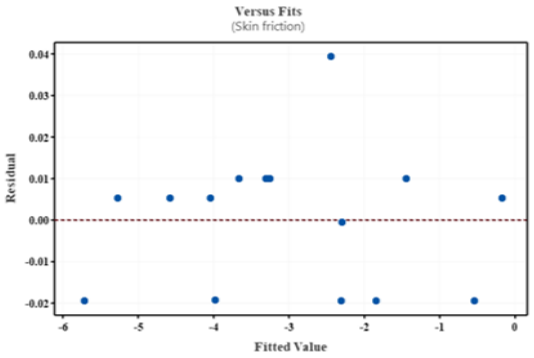

(b) Residuals vs. fitted values for $\mathbb{C}_f$

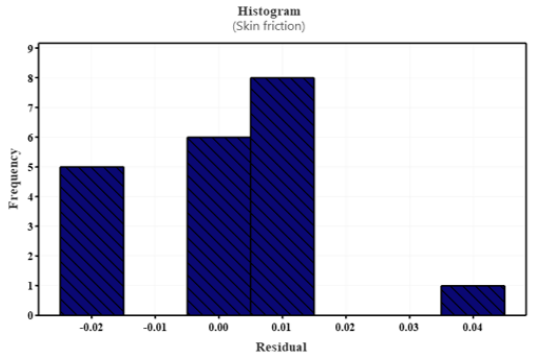

(c) Residual histogram for $\mathbb{C}_f$

(d) Residuals vs. run order for $\mathbb{C}_f$

Figure 3: .

Sensitivity Analysis for Skin Friction

The sensitivity of the response (C_f) (when sb=0) is presented in Table 5. The results show the variation in sensitivity coefficients

$$\left(\frac{\partial Sf}{\partial We}, \frac{\partial Sf}{\partial sb}, \frac{\partial Sf}{\partial Sr}\right)$$

across different levels of We and Sr.

sb	We	Sr	$\partial\left(C_f\sqrt{Re_x}\right)/\partial We$	$\partial\left(C_f\sqrt{Re_x}\right)/\partial sb$	$\partial\left(C_f\sqrt{Re_x}\right)/\partial Sr$
0	-1	-1	37.1495	119.8030	8.7356
0	-1	0	26.8378	15.4280	5.2972
0	-1	1	16.5261	-88.9470	1.8588
0	0	-1	26.8197	102.1850	-1.5761
0	0	0	16.5080	-2.1900	-5.0145
0	0	1	6.1963	-106.5650	-8.4529
0	1	-1	16.4899	84.5670	-11.8878
0	1	0	6.1782	-19.8080	-15.3262
0	1	1	-4.1335	-124.1830	-18.7646

Table 5: **Sensitivity analysis of the response (C_f) when sb = 0.**

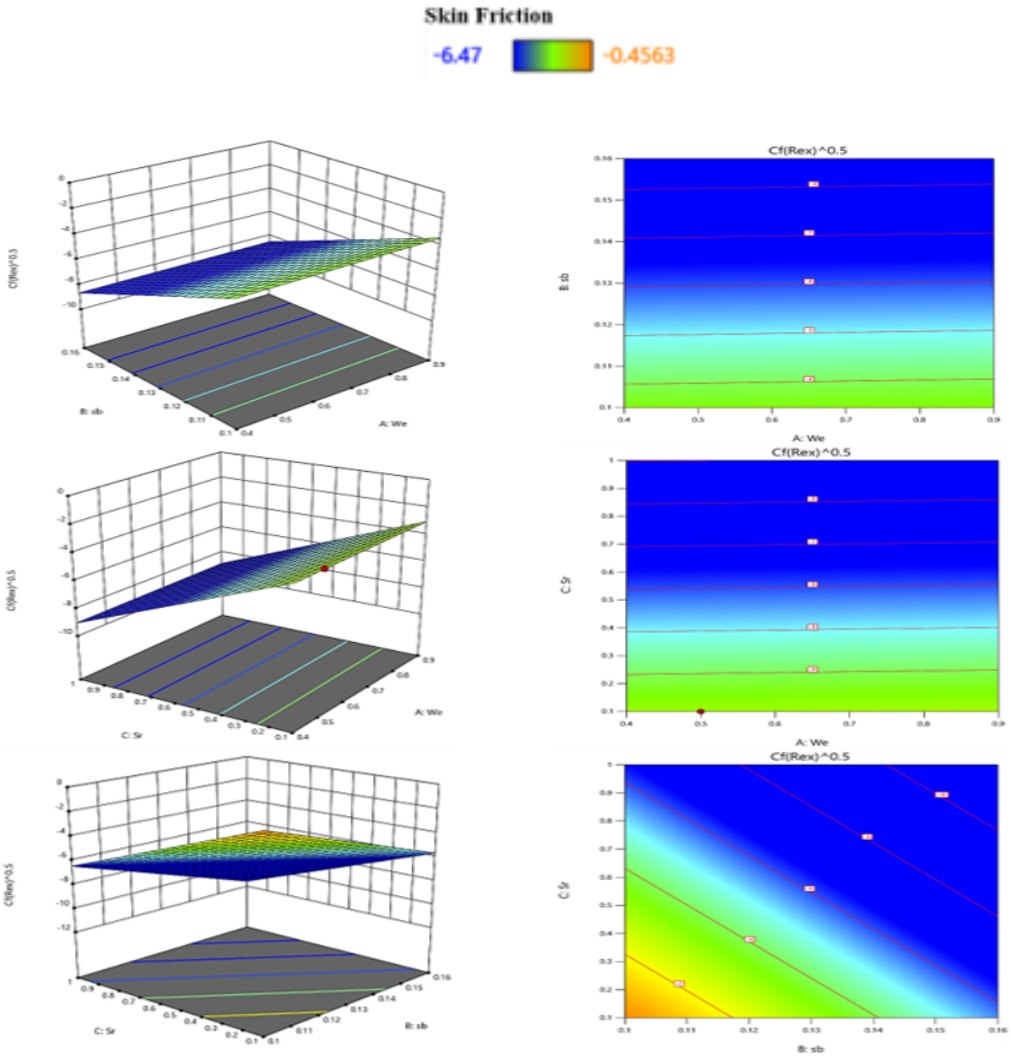

Figure 4: **Surface and Contour plot for $\mathbb{C}_f$**

The three-dimensional response surface plots and the contour plots of the skin friction coefficient $\mathbb{C}_f$ are shown in Figure 4 to demonstrate the overall influence of the controlling parameters We (A), sb (B), and Sr (C). These plots can be used to clearly visualize the individual and interactive effects of the parameters on wall shear stress behavior. Based on the surface plots, the skin friction coefficient is strongly influenced by variations in the Williamson parameter (We), Stefan parameter (sb), and Soret number (Sr). Specifically, a higher Williamson parameter (We) typically reduces the scale of skin friction. Physically, this effect can be explained by the shear-thinning property of the Williamson fluid: higher values of We reduce the effective viscosity at the wall, thereby reducing the resistance to flow and wall shear stress.

The Stefan parameter (sb), which accounts for the effect of phase change or the transfer of thermal energy, is also important. A rise in sb increases thermal activity within the surface area that may change the velocity gradients and thus affect the skin friction. This implies that heat transfer and momentum transfer are highly coupled. On the same note, the Soret number (Sr), which is related to thermal diffusion, influences mass transfer driven by temperature differences. An increase in Sr will change concentration distributions, which will subsequently affect fluid density and viscosity, ultimately affecting the shear stress at the wall. These interactions are also supported by the contour plots, in which the curvature of the contour lines and their orientation reveal strong nonlinear effects and interactions among the parameters.

The curved and tilted nature of the response surfaces indicates strong interaction effects, especially among (We–sb), (We-Sr), and (sb-Sr). The non-parallelism of the contour lines supports the ANOVA results, which show that the parameters do not interact with each other but rather with skin friction behavior. In practice, these findings are significant in real-time applications in biomedical systems and engineering. As an example, the parameters Sr and we can be used to control wall shear stress in blood flow through stenosed arteries modeled as non-Newtonian fluids, a factor vital for avoiding arterial damage or plaque rupture. Similarly, in industrial operations involving heat and mass transfer (such as polymer processing or cooling systems), knowledge of these interactions can be used to optimize operating conditions, reduce energy losses, and enhance efficiency. On balance, Figure 4 provides both statistical and physical insight into the complex interactions among the governing parameters, thereby justifying the efficiency of response surface methodology in describing nonlinear fluid behavior and assisting design optimization.

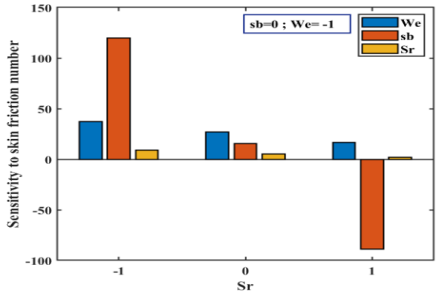

(a) Sensitivity bar graph for $\mathbb{C}_f$ with respect to We (A).

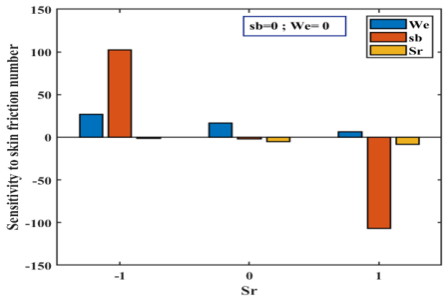

(b) Sensitivity bar graph for $\mathbb{C}_f$ with respect to sb (B).

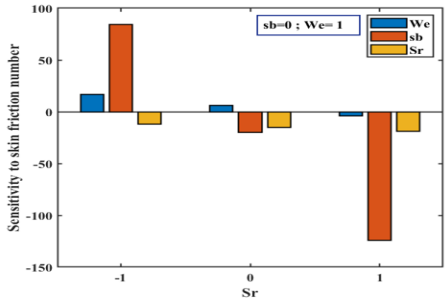

(c) Sensitivity bar graph for $\mathbb{C}_f$ with respect to Sr (C).

Figure 5: Sensitivity Bar Graphs for $\mathbb{C}_f$

Figures 5 show bar graphs of the sensitivity of the skin friction coefficient $\mathbb{C}_f$ to the operating parameters and provide a quantitative indication of the effect of changes in each operating parameter on the response under varying conditions. Figure 5a shows the $\mathbb{C}_f$ sensitivity to the Williamson parameter We (A). We find that variations significantly influence skin friction because they directly govern the fluid's non-Newtonian behavior. Physically, we increase the shear-thinning effect, which decreases the effective viscosity in a region close to the wall. This reduces velocity gradients and, by extension, the shear stress on the walls. Thus, the sensitivity pattern indicates the degree to which the fluid's rheological characteristics control momentum transport.

The sensitivity of $\mathbb{C}_f$ with respect to Stefan parameter sb (B) is shown in Figure 5b. The findings suggest that the effect of sb is very unpredictable with relation to the values of other parameters. Opacities of $\mathbb{C}_f$ to sb are highly positive at low values of We and Sr, indicating that as the thermal effects increase, the velocity gradients near the wall are reinforced, thereby increasing skin friction. The sensitivity, however, is very negative at higher values of We and Sr. The physical explanation of this reversal is that the effects of shear-thinning and thermal diffusion dominate and cause the fluid resistance to decrease and the wall shear stress to be weakened. This behavior emphasizes the nonlinear interaction between fluid rheology and thermal energy transport.

Figure 5c shows that $\mathbb{C}_f$ is sensitive to the Soret number Sr(C), which controls the effects of thermal diffusion. Temperature variations cause concentration gradients in Sr, which in turn modify the distributions of fluid density and viscosity. In certain parameter regimes, Sr augmentation increases mass diffusion, redistributing momentum in the boundary layer and altering the wall shear stress. The sensitivity trend shows that Sr is a secondary but important player, especially in interactions with We and sb. All in all, the sensitivity plots clearly indicate that the effects of each parameter cannot be considered independent, but strong interaction effects are at work. This change in the sign of sb across multiple regimes of parameter space is a strong indication of a highly nonlinear relationship among We, sb, and Sr. In practice, to operate such systems efficiently and safely, it is necessary to have accurate control of the wall shear stress.

4.2. ***Results and Discussion for Nusselt Number (Nu)***

4.3. Statistical Analysis (ANOVA):

Table 6 summarizes the results of the Analysis of Variance (ANOVA) for the Nusselt number (Nu), indicating the statistical significance and strength of the developed response surface model. The overall model is highly significant, with an F-value of 2569.03 and a corresponding p-value of 0.000, indicating that the variation explained by the model is much higher than the unexplained error. The linear terms (A, B, C), quadratic (square) terms (A2, B2, C2), and two-way interaction terms (AB, AC, BC) are all significant at the 95% confidence level (p ¡ 0.05). This establishes that individual parameters, as well as their interplay, play a significant role in determining the heat transfer properties (as reflected in the Nusselt number). Moreover, the model has remarkably good goodness-of-fit statistics, with R2 = 99.96 and adjusted R2 = 99.92, indicating that almost all variability in the response is explained by the model. This strong consistency between the expected and experimental results indicates the predictability and reliability of the generated model in analyzing and optimizing heat transfer performance.

Regression Equation in Uncoded Units:

$$\begin{aligned} Nu = {} & 4.674 - 14.735\,We + 31.07\,sb + 0.0237\,Sr \\ & + 8.6422\,We^2 - 146.62\,sb^2 + 1.3417\,Sr^2 \\ & + 18.919\,We \times sb + 2.6009\,We \times Sr \\ & - 22.882\,sb \times Sr \end{aligned} \tag{4.1}$$

4.4. Model Adequacy Checking for Nu:

Figures 6 show the residual diagnostics for the Nusselt number (Nu) model, which provide a good indication of the model's statistical validity and its ability to reflect the underlying heat transfer processes. The

Table 6: ANOVA analysis table

Source	**DF**	**Adj SS**	**Adj MS**	**F-Value**	**P-Value**	**Significant**
Model	9	8.04358	0.89373	2569.03	0.000	yes
Linear	3	0.91933	0.30644	880.87	0.000	yes
A	1	0.12981	0.12981	373.14	0.000	yes
B	1	0.66106	0.66106	1900.21	0.000	yes
C	1	0.12846	0.12846	369.26	0.000	yes
Square	3	5.51490	1.83830	5284.19	0.000	yes
A*A	1	4.20446	4.20446	12085.72	0.000	yes
B*B	1	0.25093	0.25093	721.29	0.000	yes
C*C	1	1.06375	1.06375	3057.75	0.000	yes
2-Way Interaction	3	1.60935	0.53645	1542.03	0.000	yes
A*B	1	0.16108	0.16108	463.01	0.000	yes
A*C	1	0.68491	0.68491	1968.77	0.000	yes
B*C	1	0.76337	0.76337	2194.30	0.000	yes
Error	10	0.00348	0.00035	–	–	–
Lack-of-Fit	5	0.00333	0.00067	–	–	–
Pure Error	5	0.00015	0.00003	–	–	–
Total	19	8.04706	–	–	–	–

normal probability plot (Figure 6a) and the residual histogram (Figure 6c) confirm that the residuals follow a normal distribution. Physically, it means that the variations between the predicted and experimental Nusselt numbers are caused by random fluctuations in thermal systems, including small experimental uncertainties or tiny-scale disruptions in the temperature and concentration fields. This assumes that neither systematic error nor unmodeled physical effect is affecting the heat transfer predictions.

Figure 6b, which plots residuals versus fitted values, shows no apparent pattern and a random distribution of points. This pattern supports the assumption of constant variance (homoscedasticity). Physically, it means that the model is predictable across all regimes of heat transfer, whether with weak or strong thermal gradients. Even in practice, in heat exchangers, cooling of electronic equipment, or biomedical heat transfer (e.g., thermal regulation in blood flow), this guarantees that the model is dependable when operating conditions vary.

The residual versus order plot (Figure 6d) shows no trend or cycle, indicating that the observations are independent. This implies that the past conditions and no effects of time, like thermal lag, system instability, and experimental drift, influence no experimental run. Physically, it is a manifestation of a stable thermal system in which heat transfer processes depend only on the present values of the parameters, not on their previous values.

Altogether, these diagnostic plots confirm that the RSM model of Nusselt number developed is statistically and physically consistent. This gives it greater confidence in its use to solve real-time engineering problems such as optimizing thermal systems, designing efficient cooling systems, and modeling the predictive behavior of heat transfer in complex non-Newtonian flows.

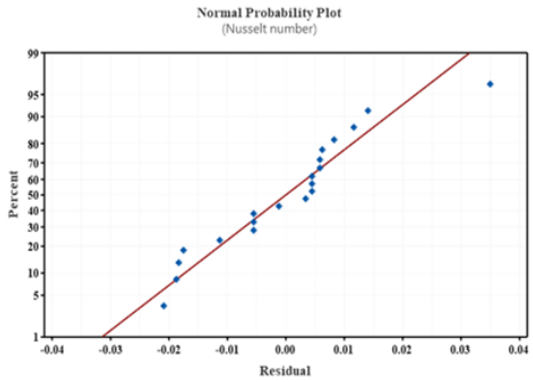

(a) Normal probability plot of residuals for Nu.

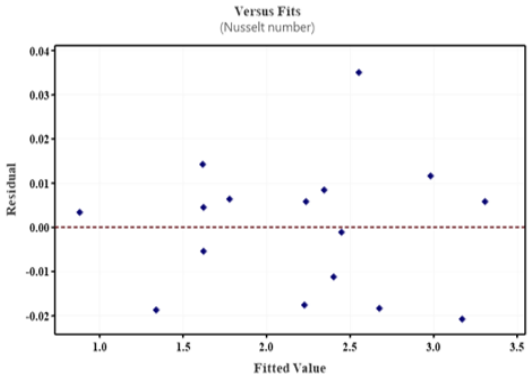

(b) Residuals vs. fitted values for Nu.

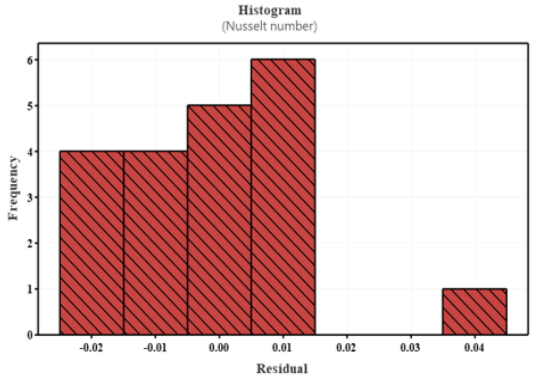

(c) Residuals histogram for Nu.

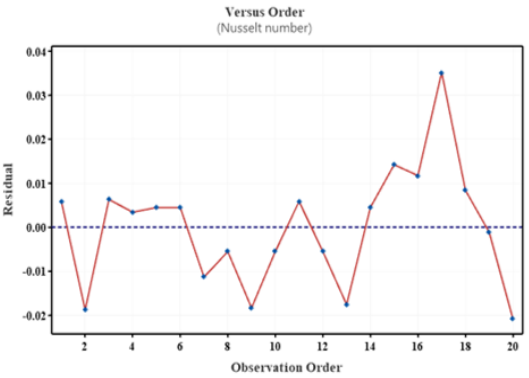

(d) Residuals vs. run order for Nu.

Figure 6: Residual Graphs

4.5. Sensitivity Analysis for Nusselt Number

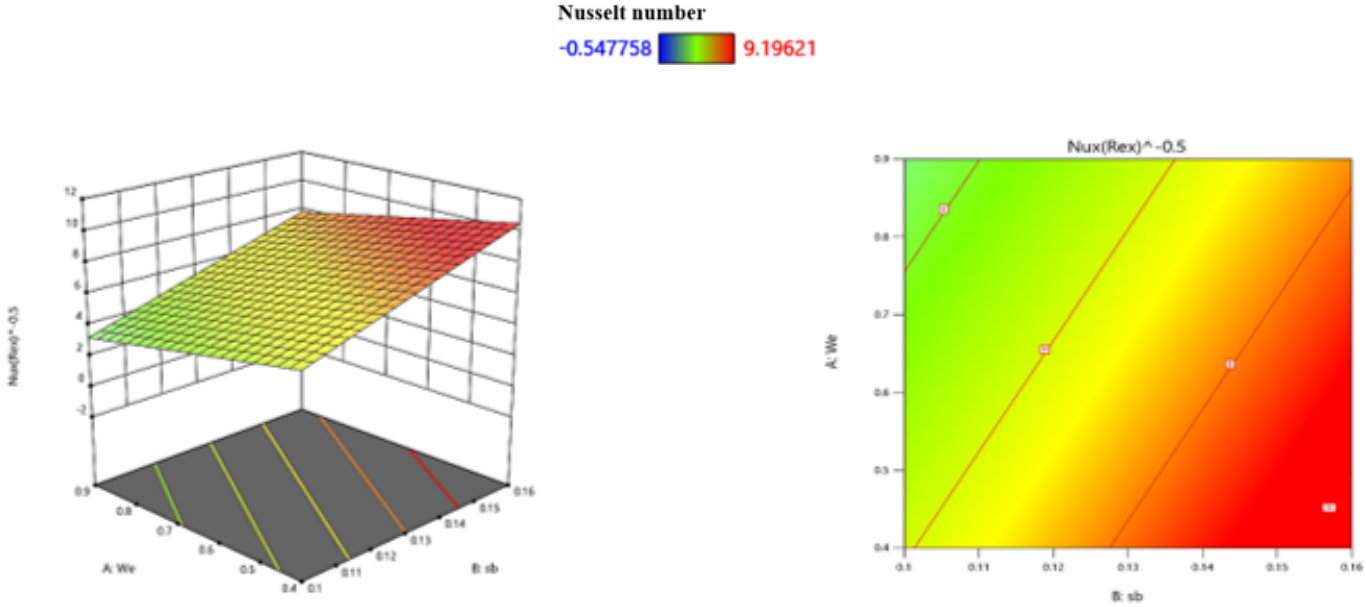

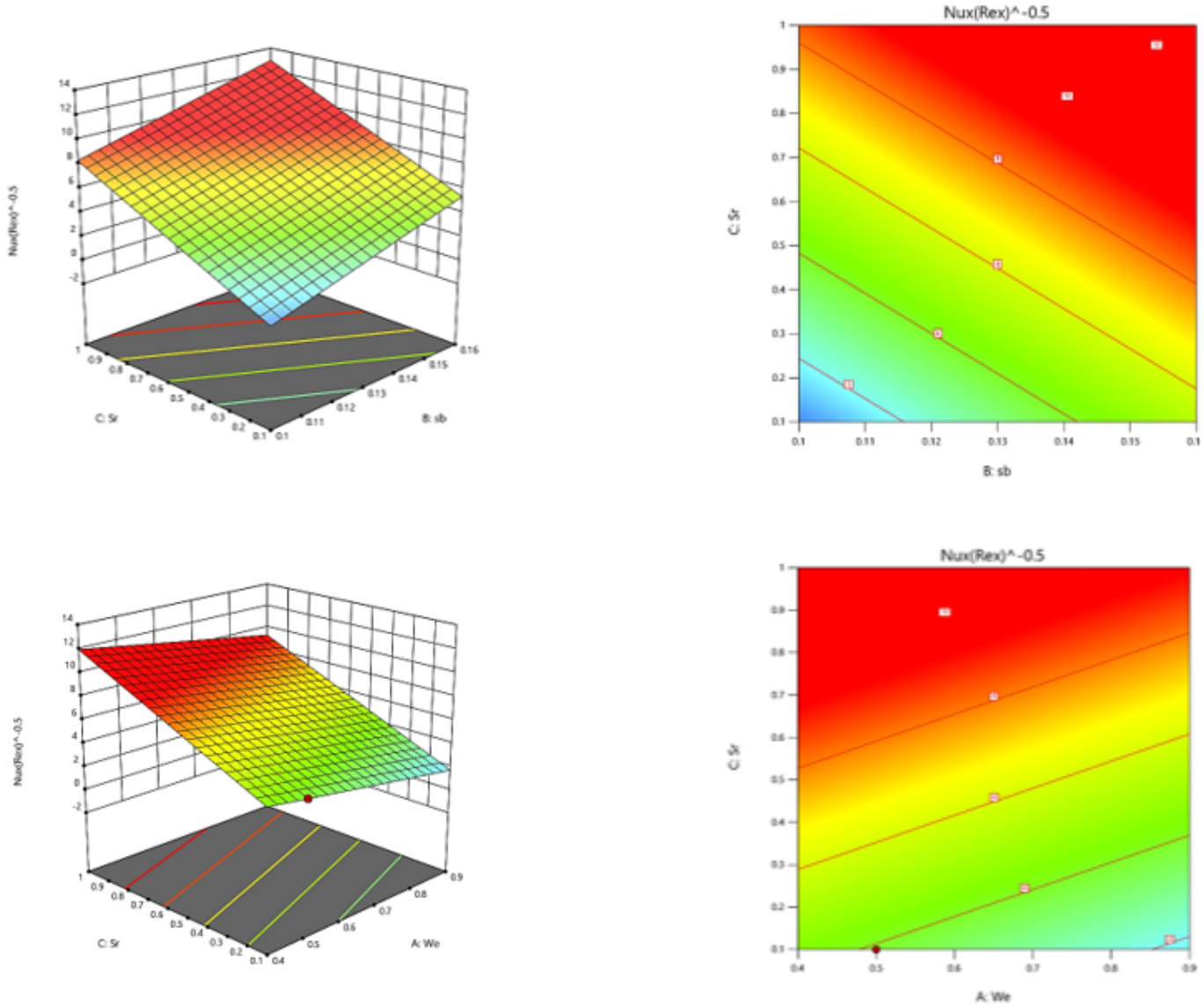

Figure 7: **Surface and Contour plot for Nu**

Table 7: **Sensitivity analysis of the response Nu when sb = 0.**

sb	*We*	*Sr*	Column 1	Column 2	Column 3
0	-1	-1	-34.6203	35.0330	-5.2606
0	-1	0	-32.0194	12.1510	-2.5772
0	-1	1	-29.4185	-10.7310	0.1062
0	0	-1	-17.3359	53.9520	-2.6597
0	0	0	-14.7350	31.0700	0.0237
0	0	1	-12.1341	8.1880	2.7071
0	1	-1	-0.0515	72.8710	-0.0588
0	1	0	2.5494	49.9890	2.6246
0	1	1	5.1503	27.1070	5.3080

Table 7 presents a comprehensive sensitivity analysis of the Nusselt number (Nu) at sb = 0, including partial derivatives of the response with respect to We, sb, and Sr. These findings provide insight into how

changes in each parameter affect heat transfer properties in the absence of phase-change effects.

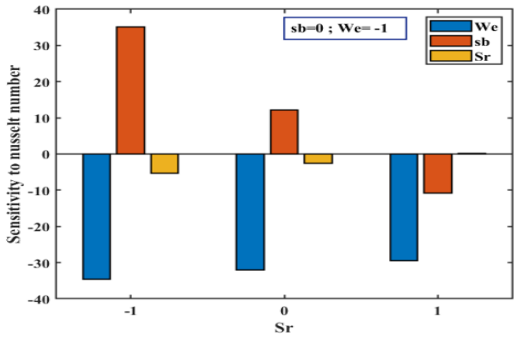

(a) Sensitivity bar graph for Nu with respect to We (A).

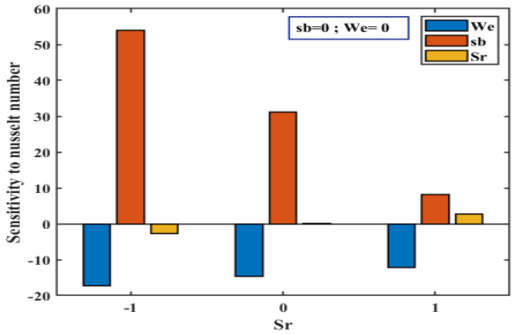

(b) Sensitivity bar graph for Nu with respect to sb (B).

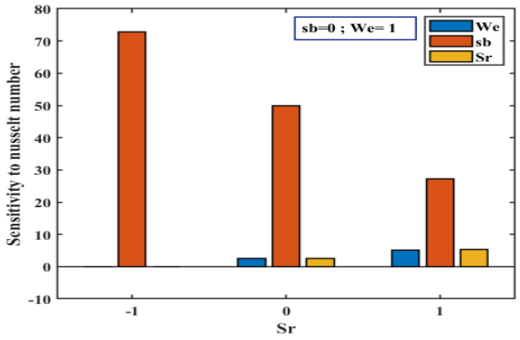

(c) Sensitivity bar graph for Nu with respect to Sr (C).

Figure 8: Sensitivity Analysis for Nu

The sensitivity of the Nusselt number (Nu) to the governing parameters is illustrated in Figures 8, providing insight into how variations in fluid properties and transport mechanisms influence heat transfer performance. Figure 8a shows the sensitivity of Nu to the Williamson parameter We (A). The sensitivity is predominantly negative across most parameter combinations, indicating that an increase in We generally reduces the heat transfer rate. Physically, this can be attributed to the shear-thinning nature of the Williamson fluid. As we increase, the effective viscosity decreases, which weakens the thermal boundary layer mixing and reduces the temperature Gradient at the wall, thereby lowering the Nusselt number. However, at higher values of both We and Sr, the sensitivity becomes positive. This reversal occurs due to enhanced coupling between momentum and mass diffusion, in which increased thermal diffusion (high Sr) promotes energy transport, compensating for the reduced viscosity and ultimately enhancing heat transfer.

Figure 8b illustrates the sensitivity of Nu to the Stefan parameter sb (B), which remains consistently positive throughout the parameter space. This indicates that increasing sb enhances the Nusselt number. From a physical standpoint, the Stefan parameter quantifies the influence of latent heat and phase-change processes. Higher values of sb intensify thermal energy exchange near the surface, leading to steeper temperature gradients and increased heat transfer rates. This consistent positive sensitivity highlights the dominant role of thermal energy transport in governing Nu.

Figure 8c presents the sensitivity of Nu to the Soret number Sr (C), which shows a transition from negative to positive values as Sr increases. At lower Sr values, thermal diffusion is weak, and its effect on heat transfer is minimal or slightly adverse due to reduced concentration-driven energy transport. However, as Sr increases, thermal diffusion becomes significant, enhancing mass flux induced by temperature gradients. This strengthens the coupling between heat and mass transfer, leading to improved thermal energy transport and an increase in the Nusselt number. Overall, these sensitivity trends demonstrate that the heat transfer process is governed by a complex interplay among non-Newtonian fluid behavior, thermal diffusion, and

phase-change effects. From a practical perspective, understanding these mechanisms is crucial in applications such as cooling systems, polymer processing, and biomedical heat transfer, where optimizing the Nusselt number is essential for improving thermal efficiency and system performance.

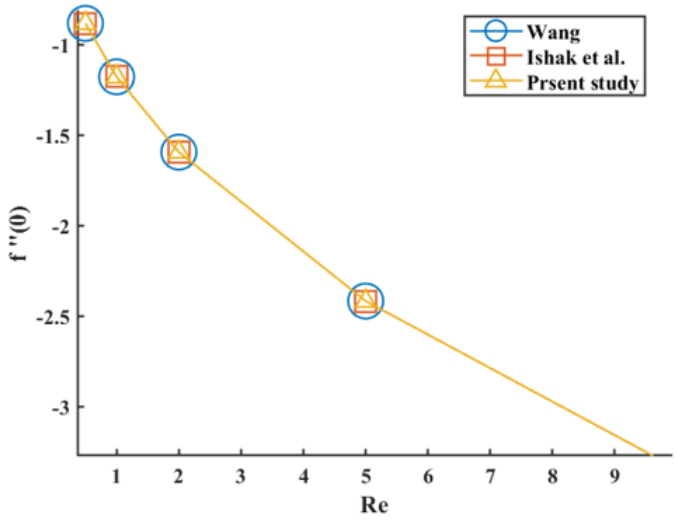

Figure 9: **Comparison plot**

To further confirm the current findings, a comparison table (Figure 9) is provided, showing good agreement with previously published studies under the same parameter conditions.

Physical mechanism behind the results

- Magnetic parameter (M): Induces Lorentz force against flow - slows down velocity, heats up through Joule heating.
- Williamson parameter (We): Strengthens shear-thinning of non-Newtonian fluids → decreases effective viscosity at high shear rates - alters velocity gradients.
- Radiation parameter (R): Intensifies the thermal energy transportation to the boundary layer, thickening the thermal boundary layer.
- Stefan parameter (sb): Phase change/heat absorption increase - increases the rate of heat transfer greatly.
- Soret number (Sr): Mass diffusion with a couple of temperature Gradient changes the concentration boundary layer.
- Interaction effects: Strong sensitivity variations in Cf and Nu are caused by the nonlinear coupling between parameters.

5. Conclusion

In this work, the non-Newtonian Williamson model is used to conduct an in-depth analysis of the tetra-hybrid nanofluid blood flow in a vertical cylinder under the joint actions of magnetohydrodynamics (MHD), thermal radiation, and ion diffusion (Soret, Dufour, and Stefan parameters). Similarity variables were used to transform the governing equations, and the equations were solved numerically. Response Surface Methodology (RSM) and sensitivity analysis were used to assess the impact and interactions of key parameters on engineering responses, including skin friction and the Nusselt number. A combination of statistical and numerical methods offers a powerful framework for understanding the complex thermo-fluid dynamics in

biomedical systems.

The key conclusions of this research are as follows:

- The RSM models derived for skin friction and Nusselt number are very accurate and statistically significant with $R^2 = 99.99\%$ and $R^2 = 99.96\%$, respectively.
- The Stefan parameter (sb) is of great importance as it contributes greatly to the way heat is transported, which means that it plays the dominant role in the mechanism of heat transfer.
- The Williamson parameter (We) has a very strong effect on the behavior of momentum since it makes the flow resistant to non-Newtonian effects.
- The Soret parameter (Sr) is a factor that adds to the coupled mass and heat diffusion, which influences the concentration and temperature fields.
- Vibrant nonlinear interaction effects, especially between (We, Sr) and (sb, Sr), have a substantial effect on skin friction and heat transfer.
- The magnetic parameter (M) slows velocity profiles caused by the Lorentz force and heats the temperature caused by Joule heating.
- The thermal radiation improves the temperature distribution, resulting in an increased thickness of the thermal boundary layer.
- Sensitivity analysis done proves that sb is the most powerful parameter on the heat transfer, and we dominate flow properties.

All in all, the research presents an effective predictive and optimization model for sophisticated biomedical applications involving intricate nanofluid flows.

Future Work

- Generalize the model to pulsatile and unsteady blood flow.
- Incorporate chemical reactions and biological factors.
- Validate results using experimental or clinical data.
- Use machine learning models to predict optimization.
- Explore the effects of entropy generation and irreversibility in a study.
- Investigate various nanoparticle mixtures and volume fractions.
- Explore patient-specific arterial geometries with imaging information.

Data Availability Statement

The data that support the findings of this study are available from the corresponding author upon reasonable request

Nomenclature

Table 8: Nomenclature

Symbol	Description	Unit
Dimensional Variables		
u, w	velocity components (axial and radial)	m/s
r, z	cylindrical coordinates	m
T	fluid temperature	K
T_w	wall temperature	K
T_∞	ambient temperature	K
C_w	concentration at the wall	kg/m^3
C_∞	ambient concentration	kg/m^3
B_0	applied magnetic field strength	$kg/(A.s^2)$
Γ	Williamson parameter	s
α	radius of curvature	m
Thermophysical Properties		
ρ_{tethnf}	density of tetra hybrid nanofluid	kg/m^3
μ_{tethnf}	dynamic viscosity of tetra hybrid nanofluid	kg/(m.s)
σ_{tethnf}	electrical conductivity of tetra hybrid nanofluid	S/m
k_{tethnf}	thermal conductivity of tetra hybrid nanofluid	W/(mK)
c_p	specific heat capacity	J/(kg.K)
D_{tethnf}	mass diffusivity	m^2/s
σ^*	Stefan–Boltzmann constant	$W/(m^2.K^4)$
Dimensionless Variables		
$f(\eta)$	stream function	–
$\theta(\eta)$	temperature	–
$\phi(\eta)$	concentration	–
η	similarity variable	–
Dimensionless Parameters		
M	magnetic parameter	–
We	Williamson parameter	–
Pr	Prandtl number	–
Sc	Schmidt number	–
Ec	Eckert number	–
R	radiation parameter	–
Engineering Quantities		
Nu_x	local Nusselt number	–
Sh	Sherwood number	–
C_f	skin friction coefficient	–

References

[1] W. Adel, H. Günerhan, K. S. Nisar, P. Agarwal, and A. El-Mesady. Designing a novel fractional order mathematical model for covid-19 incorporating lockdown measures. *Scientific Reports*, 14(1):2926, 2024. 1

[2] P. Agarwal, S. S. Deniz, S. Jain, A. A. Alderremy, and S. Aly. A new analysis of a partial differential equation arising in biology and population genetics via semi-analytical techniques. *Physica A: Statistical Mechanics and its Applications*, 542:122769, 2020. 1

[3] P. Agarwal, F. Hubert, Y. Dermenjian, U. Baltaeva, and B. Hasanov. The cauchy problem for the heat equation with a fractional load. *Discrete and Continuous Dynamical Systems-S*, 0(0):0–0, 2024. 1

[4] M. Al-Dhaifallah, K. S. Nisar, P. Agarwal, and A. Elsayyad. Modeling and identification of a heat exchanger process using least-squares support vector machines. *Thermal Science*, 21(6 Part B):2859–2869, 2017. 1

[5] M. M. Ali, R. Akhter, and M. A. Alim. Thermal performance of hybrid nanofluid mixed convective flow in a horizontal channel equipped with dimpled surfaces and a rotating solid cylinder subjected to a magnetic field: Sensitivity analysis. *South African Journal of Chemical Engineering*, page 100838, 2026. 1

[6] S. U. Choi. Enhancing thermal conductivity of fluids with nanoparticles. In *ASME International Mechanical Engineering Congress and Exposition*, volume 17421, pages 99–105. American Society of Mechanical Engineers, 1995. 2.4, 2.5

[7] Y. M. Chu, N. Ali Shah, P. Agarwal, and J. Dong Chung. Analysis of fractional multi-dimensional Navier–Stokes equation. *Advances in Difference Equations*, 2021(1):91, 2021. 1

[8] S. K. Das, S. U. Choi, W. Yu, and T. Pradeep. *Nanofluids: Science and Technology*. John Wiley & Sons, 2007. 2.4, 2.5

[9] J. A. Eastman, S. U. S. Choi, S. Li, W. Yu, and L. J. Thompson. Anomalously increased effective thermal conductivities of ethylene glycol-based nanofluids containing copper nanoparticles. *Applied Physics Letters*, 78(6):718–720, 2001. 2.4, 2.5

[10] S. D. Farahani, M. Hossieni, and A. A. Alizadeh. Performance prediction of concentrated photovoltaics with mini-channel and elastic cylinders using anfis and sobol sensitivity analysis. *Renewable Energy*, 256:123889, 2026. 1

[11] Y. C. Fung. *Biomechanics: Mechanical Properties of Living Tissues*. Springer Science & Business Media, 2013. 2.4, 2.5

[12] W. M. Haynes. *CRC Handbook of Chemistry and Physics*. CRC Press, 2016. 2.4, 2.5

[13] M. Irfan, T. Muhammad, M. Rashid, M. S. Anwar, S. S. Abas, and P. S. Narayana. Numerical study of nonlinear thermal radiation and joule heating on mhd bioconvection carreau nanofluid with gyrotactic microorganisms. *Journal of Radiation Research and Applied Sciences*, 18(1):101254, 2025. 2

[14] N. Jamal, M. Sarwar, P. Agarwal, N. Mlaiki, and A. Aloqaily. Solutions of fuzzy advection-diffusion and heat equations by natural adomian decomposition method. *Scientific Reports*, 13(1):18565, 2023. 1

[15] K. B. Kasali and S. O. Ajadi. Sensitivity and numerical investigations of an mhd elastico-viscous hybrid nanofluid flow between two rotating disks. *Multiscale and Multidisciplinary Modeling, Experiments and Design*, 9(1):108, 2026. 1

[16] N. Khan, M. Farooq, W. U. Jan, R. Jan, P. Agarwal, and I. Ahmad. Unsteady flow of carbon nanotube-based hybrid nanofluid with joule heating, viscous dissipation, and homogeneous–heterogeneous reactions. *International Journal of Applied and Computational Mathematics*, 11(6):252, 2025. 1

[17] S. Panda, S. Ontela, S. R. Mishra, and P. K. Pattnaik. A statistical model on heat transportation of hybrid magnetic nanoparticles with slip constraints on a heated shrinking sensor device using analysis of variance: sensitivity analysis. *Numerical Heat Transfer, Part A: Applications*, 87(1):2365995, 2026. 1

[18] C. Parida, D. Mohanty, G. Mahanta, and S. Shaw. Thermo-solutal impact of mhd hybrid nanofluid flow containing gyrotactic microorganisms over an inclined cylinder. *Numerical Heat Transfer, Part A: Applications*, 87(1):2541813, 2026. 1

[19] S. C. Ramamoorthi, P. Reddy, and K. A. Kumar. Response surface and sensitivity analysis of entropy generation in casson hybrid nanofluid flow through a stenosed artery. *Multiscale and Multidisciplinary Modeling, Experiments and Design*, 9(1):38, 2026. 1

[20] S. Rashid, K. T. Kubra, S. Sultana, P. Agarwal, and M. S. Osman. An approximate analytical view of physical and biological models in the setting of the caputo operator via the elzaki transform decomposition method. *Journal of Computational and Applied Mathematics*, 413:114378, 2022. 1

[21] A. Rehman, M. Inc, E. Jawo, and K. Sudarmozhi. Analytical solution of marangoni convection flow of ethylene glycol-based nanofluid with heat transfer analysis. *International Journal of Thermofluids*, page 101462, 2025. 1

[22] A. Rehman, A. A. Saad, M. Inc, S. S. Abas, N. S. Khashi'ie, S. Rezapour, and K. Sudarmozhi. Significance of heat transfer in coupled mhd hybrid nanofluid over a surface embedded in porous medium with thermal radiation and viscous dissipation. *Journal of Engineering Research*, 2026. 1

[23] M. Shams, N. Kausar, C. Samaniego, P. Agarwal, S. F. Ahmed, and S. Momani. An efficient fractional caputo-type simultaneous scheme for finding all roots of polynomial equations with biomedical engineering applications. *Fractals*, 31(04):2340075, 2023. 1

[24] M. Shoaib, T. Javed, and B. Iftikhar. Sensitivity analysis of mhd casson hybrid nanofluid and heat transfer with joule heating. *Multidiscipline Modeling in Materials and Structures*, 22(1):192–217, 2026. 1

[25] K. Sudarmozhi, V. S. Devi, G. Rasool, L. A. El Maati, M. Alomar, and S. G. Tawfik. Isothermal behavior and streamline visualization of a tetra-hybrid nanoparticle suspension in water-based williamson fluid under the influence of the stefan effect. *Tribology International*, page 111365, 2025. 1

[26] X. Zhang, P. Agarwal, Z. Liu, and H. Peng. The general solution for impulsive differential equations with riemann-liouville fractional-order $q \in (1, 2)$. *Open Mathematics*, (1), 2015. 1